Corrosion Science 213 (2023) 110952

Contents lists available at ScienceDirect

Corrosion Science

journal homepage: www.elsevier.com/locate/corsci

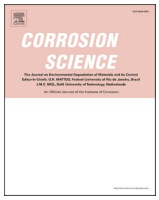

Adsorption mechanism of quaternary ammonium corrosion inhibitor on carbon steel surface using ToF-SIMS and XPS

Luntao Wang [a,1], Huiru Wang [b,c,1], Antoine Seyeux [a], Sandrine Zanna [a], Alain Pailleret [c], Srdjan Nesic [b], Philippe Marcus [a,*]

[a] Université PSL, CNRS – Chimie ParisTech, Institut de Recherche de ChimieParis, Groupe Physico-Chimie des Surfaces, 75005 Paris, France
[b] Institute for Corrosion Multiphase Technology, Ohio University, Athens OH 45701, USA
[c] Sorbonne Université, CNRS, Laboratoire Interfaces et Systèmes Electrochimiques (LISE, UMR 8235), 4 place Jussieu, (case courrier 133), 75005 Paris, France

ARTICLE INFO

Keywords:
Quaternary ammonium
Carbon steel
Corrosion inhibitor
CO_2 corrosion
ToF-SIMS
XPS

ABSTRACT

ToF-SIMS and XPS are combined to study the adsorption of tetradecyl-benzyldimethyl-ammonium (BDA-C14) bromide corrosion inhibitor on carbon steel surface. BDA-C14 forms a protective layer with N-containing polar head group interacting with carbon steel surface. The adsorbed inhibitor surface coverage strongly depends on immersion time and inhibitor concentration. A maximum and uniform coverage is found for sufficiently long exposure times at a critical inhibitor concentration of about 25 ppm_w. The uniform adsorbed inhibitor layer formed on the surface mitigates the formation of iron chloride/hydroxide intermediates and thus enhances the corrosion protection of carbon steel in aggressive environment.

1. Introduction

For fast and convenient operation and large transportation volume of crude oil and natural gas, pipelines are an economical key answer to the continuous demand for oil and gas [1]. Pipelines are commonly produced out of carbon steel due to their good mechanical properties and low cost [2,3]. However, it is known that carbon steel suffers from high corrosion risks in aggressive environments, which makes the internal pipeline corrosion a challenging problem and may cause huge economic losses and safety issues [1,4]. Among the available corrosion mitigation methods, the use of corrosion inhibitor is the most cost-efficient and convenient way to slow down the internal pipeline corrosion rate [5].

Organic inhibitors protect the metallic substrate by forming an adsorbed layer which can impede the access to the surface by water molecules and other corrosive species [6]. The inhibition effectiveness depends on the ability of the inhibitor / surface system to form an adherent and continuous layer. The polar functional headgroups and the intermolecular interactions between the inhibitor molecule tails play a crucial role [7,8]. Based on the interaction strength between surface and inhibitor, the inhibitor compounds have been described as being physisorbed or chemisorbed [9]. Physisorption describes the weak electrostatic interactions between charged substrate/inhibitor molecules, as well as van der Waals interactions, dipole-dipole and London forces [9]. Heteroatoms contained in the polar headgroups, such as N, P, O, and/or S of imidazolines, phosphate esters, quaternary ammonium compounds and thiols, usually act as adsorption centers [9–12]. Some organic inhibitors can adsorb on the carbon steel surface by sharing conjugative bonding or π-electrons between the inhibitor and metallic d-orbital, leading to stronger bonds, which is often referred to as chemisorption [10,13,14]. The heterocyclic compounds containing S atom often exhibit good corrosion inhibition performance because they have high-density electron clouds around the substitutive atoms/groups on the ring, which makes them interact with the metal surface more readily, leading to chemisorption [6]. With chemisorption that involves charge sharing or charge transfer between inhibitor molecule and metal surface, the resulting adsorption is stronger and more persistent. Although chemisorption usually provides strong interactions with surfaces, it may have slow adsorption kinetics [15,16] and has large chemical specificity meaning that the occurrence of chemisorption strongly depends on the type of surface [16–18]. In contrast, physisorption provides weaker interaction with surfaces, but adsorption kinetics is faster and is not as sensitive to the surface type [16,19–21].

Previous studies of organic inhibitors have been mostly focused on exploring corrosion inhibition efficiency by electrochemical methods.

* Corresponding author.
E-mail address: philippe.marcus@chimieparistech.psl.eu (P. Marcus).
[1] Indicates equal contribution.

https://doi.org/10.1016/j.corsci.2022.110952
Received 30 September 2022; Received in revised form 26 December 2022; Accepted 30 December 2022
Available online 3 January 2023

Potentiodynamic polarization curves and electrochemical impedance spectra have been the most commonly used techniques for investigating organic inhibitor performance. By measuring the inhibitor layer capacitance, double layer capacitance, and charge transfer resistances using electrochemical impedance spectroscopy, the inhibitor layer structures and corrosion rates were estimated [22–26]. By measuring the variations of corrosion rates with the increase in inhibitor concentration at various temperatures, it was found that experimental data on inhibition studies can be described in terms of adsorption isotherms, by using Langmuir, Temkin or Frumkin models. In addition, by monitoring the positive or negative shifts of corrosion potential after adding inhibitors, some researchers proposed a selective inhibitor adsorption on anodic or cathodic sites where inhibitor preferentially retarded the anodic or cathodic reactions [27,28]. Take the widely used quaternary ammonium inhibitor for example, some authors claimed that it mainly mitigates the anodic reaction by preferential adsorption on anodic sites, as indicated by the positive shift of corrosion potential [28,29]. However, this interpretation cannot be assumed valid for the conditions where a limiting current controls the cathodic reaction or passive current controls the anodic reaction. On the other hand, Dominguez et al. pointed out that a positive shift of corrosion potential does not mean that the added inhibitor preferable retards the anodic reaction. They gave a more comprehensive interpretation in which one can see a positive shift of the corrosion potential when the corrosion process is initially under mixed or limiting current control, even if both anodic and cathodic charge transfer reactions are equally retarded, whereas the limiting current is not [30].

These contradictions and discrepancies could be, at least in part, attributed to the limitation of traditional electrochemical techniques. The corrosion inhibition behaviour of organic inhibitor greatly depends on the metal-solution interface, which can strongly affect the adsorption properties. The commonly used electrochemical techniques only focus on the electrochemical process reactions and provide no or little direct evidence on surface adsorption. The use of advanced surface analysis techniques such as atomic force microscopy (AFM) [31–33], scanning tunnelling microscopy (STM) [34], X-ray photoelectron spectroscopy (XPS) [35–40] and time-of-flight secondary ion mass spectrometry (ToF-SIMS) [36–39] have greatly contributed to a better understanding of inhibitor adsorption. The XPS and ToF-SIMS techniques are particularly appropriate to analyse the chemical structure of thin surface layers in corrosion studies [36,37,41,42]. A few XPS and ToF-SIMS studies have been performed in the past to study corrosion inhibitors on brass [38,39], copper [35], and aluminium [36,37]. For example it was found by XPS that, on brass, an organometallic complex forms on top of a surface layer [38]. XPS can also identify the surface inhibitor density through detecting the N-containing (inhibitor related) species on aluminium or brass by principal component analysis or by quantitative high resolution XPS data analysis [37,38]. ToF-SIMS can be used as a powerful technique to analyse the inhibitor bonding mechanism, the distribution of inhibitor molecules in the surface layer, and the thermal stability of surface layer, as already reported on aluminium [36,38,39].

Only few studies of corrosion inhibition of carbon steel using XPS and ToF-SIMS techniques have been found [43–45]. In the present work, both XPS and ToF-SIMS techniques were employed to explore the adsorption and inhibition mechanisms of a quaternary ammonium model compound on an extensively used UNS G1018 carbon steel in CO_2 saturated NaCl solution.

2. Experimental

2.1. Substrate material and chemicals

UNS G1018 steel specimen, which consist of 0.018 % C, 0.75 % Mn, 0.011 % P, 0.021 % S and 0.0067 % N and Fe in balance, were cut out in a form of a 1–3 mm thick flat square sheet with 1 × 1 cm^2 area. These carbon steel specimens were polished using 600, 1200, 2400, and 4000 SiC papers, and then polished down to 0.25 μm with alumina oxide suspensions. The polished specimens were finally thoroughly rinsed with distilled water and quickly dried under a stream of compressed air.

The organic corrosion inhibitor used in this work was a model quaternary ammonium compound which contains a polar headgroup, dimethylbenzylammonium and a hydrophobic tail consisting of 14 carbon atoms-tetradecyl (-$C_{14}H_{17}$), and the counterion is bromide. This model compound (BDA-C14) was synthesized in-house in order to reach a high level of purity (99 %), necessary to precisely investigate the role of the headgroup and tail during adsorption and corrosion inhibition. The purity of this BDA-C14 model compound was characterized by proton nuclear magnetic resonance (^{1}H NMR or simply NMR). The molecular structure of this model compound is illustrated in Fig. 1. The details of the synthesis process of this compound were presented in previous publications [46,47].

Aqueous 1 wt% NaCl solution containing different concentrations of BDA-C14 were used as corrosive medium, which are typically used for representing water environment with dissolved salt in oil and gas fields. The BDA-C14 inhibitor is completely soluble at all test concentrations in aqueous solutions. The solubility of BDA-C14 in 1 wt% NaCl is larger than 500 ppm_w (parts per million by weight, equivalent to mg/L). The solutions were prepared using deionized water with a resistivity of 18 MΩ.cm. Before specimen immersion, the solution was purged by CO_2 bubbling for at least 2 h to remove dissolved oxygen and saturate the solution.

2.2. Immersion test

Immersion tests were carried out in 50 mL glass vials at room temperature (25 ± 2 °C). CO_2 atmosphere was continuously maintained during the specimen immersion. The inhibitor concentrations used in immersion tests were 0, 5, 10, 25, and 100 ppm_w. The initial pH of the test solution was 3.9 ± 0.1. The immersion times were 3, 10, 20 min, 1 h, and 3 h. After immersion, the specimen was taken out, rinsed by distilled water, dried in a stream of CO_2 gas and introduced in XPS and ToF-SIMS chambers where they were analysed.

2.3. Surface analysis

Time-of-flight secondary ion mass spectrometry measurements were performed using a dual beam ToF-SIMS V spectrometer (IONTOF GmbH, Muenster, Germany). The base pressure in the analysis chamber is maintained below 5.0 × 10^{-9} mbar in normal operating conditions. The total primary ion flux was less than 10^{12} ions cm^{-2} to ensure static conditions. For mass spectra measurements, the spectrometer was run in high-current bunched mode for optimum mass resolution (M/ ΔM about 8000). A Bi^+ primary ion source with a 1.2 pA current, scanned over a 500 × 500 μm^2 square area (45° incidence to the specimen surface) was used as the analysis beam. Each specimen was analysed at least four

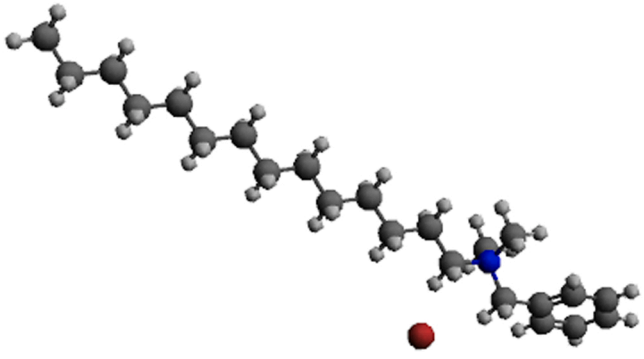

Fig. 1. The molecular structure of tetradecyl-benzyldimethyl-ammonium (BDA-C14) bromide.

times on different areas. Depth profiles measurements were performed in high-current bunched mode with dual beam using a pulsed 25 keV Bi^+ primary ion source delivering 1.2 pA of target current over a 100 × 100 μm^2 area (45° incidence to the specimen surface) interlaced with a 500 eV Cs^+ sputter beam delivering 25 nA of target current over a 300 × 300 μm^2 area (45° incidence to the specimen surface). Both the positive and negative depth profiles were recorded (remark: ToF-SIMS being a destructive technique, positive and negative profiles have been obtained in two distinct areas). Since ToF-SIMS is a non-quantitative technique (due to a strong matrix effect on ion emission), the intensity of the plotted ions cannot be compared directly and do not reflect the concentrations of the associated species in the substrate. However, ToF-SIMS mass spectra and depth profiles can be used to evaluate the intensity evolution for a given ion if the matrix remains similar. Thus, when a comparison between two specimens is done for a similar matrix, it is considered that the ionization yield is similar for the two specimens. In this study, we assume that the ionization yields of the inhibitor on the specimen surface remain similar, making the comparison of the intensities of same ions between ToF-SIMS mass spectra and depth profiles possible to evaluate the composition variation as function of the immersion time and inhibitor concentrations.

X-ray photoelectron spectroscopy analysis was performed using a Thermo Electron ESCALAB 250 spectrometer. A monochromated Al Kα X-ray source ($h\nu$ = 1486.6 eV) was used. The base pressure in the analytical chamber was maintained at 10^{-9} mbar. The take-off angle was 90° and the XPS analysed surface is a disk area with 500 μm diameter. Survey spectra were recorded with a pass energy of 100 eV at a step size of 1 eV and high-resolution spectra were recorded with a pass energy of 20 eV at a step size of 0.1 eV.

3. Results and discussion

Fig. 2 shows the ToF-SIMS positive ion spectrum for BDA-C14 inhibitor, which was deposited on a silicon wafer by immersion in inhibitor saturated ultra-pure water, recorded between m/z = 0 and 340. This spectrum was obtained with sufficiently low primary ion current, providing static conditions, so that only the first layers of the specimen surface are probed (between 1 and 3 monolayers). Typical hydrocarbon related peaks, i.e., C^+ at m/z 12.00, CH^+ at m/z 13.00, $C_2H_3^+$ at m/z 27.02, $C_3H_5^+$ at m/z 41.04 and $C_7H_7^+$ at m/z 91.05, are labelled in the spectrum [39]. The origin of these hydrocarbon peaks at low mass range is twofold: ionization of carbonaceous contamination from transfer in air of the specimen, and fragmentation of BDA-C14 inhibitor present on the surface. A good proof of the presence of BDA-C14 inhibitor on the surface is the signal of the molecular ions $C_{16}H_{34}N^+$ (m/z = 240.27) and $C_{23}H_{42}N^+$ (m/z = 332.32) which correspond to the functional headgroup containing the heteroatom N the alkyl tail comprised of 14 carbon atoms, and the whole inhibitor molecule, respectively.

Fig. 3 shows the ToF-SIMS mass spectra recorded for the carbon steel surfaces after 1 h immersion in 1 wt% NaCl solution with various concentrations of BDA-C14 inhibitor (0, 5, 10, 25, and 100 ppm_w). From 0–25 ppm_w the intensities of $C_{16}H_{34}N^+$ and $C_{23}H_{42}N^+$ signals increase from about a negligible value to about 5 × 10^5 and 4 × 10^6 counts. For higher inhibitor concentration (100 ppm_w), the intensities of the characteristic $C_{16}H_{34}N^+$ and $C_{23}H_{42}N^+$ ions remain identical to those observed for 25 ppm_w (around 5 × 10^5 and 4 × 10^6 counts). This shows that (i) increasing inhibitor concentration in the solution lead to a higher level of inhibitor adsorption on the carbon steel surface, and (ii) the adsorption of inhibitor on the surface reaches a saturation level for about 25 ppm_w concentration, indicating that the maximum surface coverage by the inhibitor was reached. Interestingly, this surface saturation phenomenon has also been observed during electrochemical corrosion rate measurements [33,47]. It was found that the stabilized corrosion rates with inhibition usually decreased as inhibitor concentrations increased until the surface was saturated with inhibitor, and any further addition of the inhibitor to the bulk solution did not lead to a measurable/significant further decrease of the corrosion rates. The value of surface saturation concentration obtained here from the ToF-SIMS mass spectra is in qualitative agreement with the saturation concentration of the same inhibitor model compound obtained by electrochemical methods (25 ppm_w −50 ppm_w) [33,47].

In order to better understand the effect of inhibitor concentration on the corrosion protection of the carbon steel in 1 wt% NaCl solution saturated with CO_2, and to elucidate the possible development of multilayers stacks of inhibitor on the carbon steel surface after immersion in high inhibitor concentration solutions (> 25 ppm_w), ToF-SIMS depth profiles for negative and positive ions were recorded. Fig. 4 summarizes the depth profiles for a compilation of fragments originating from negative (Cl^-, FeO_2^- and Fe_2^-) and positive ($C_{16}H_{35}N^+$ and $C_{23}H_{42}N^+$) ions for various inhibitor concentrations. Negative and positive profiles are not recorded on the same area, but on the same specimen, so they are plotted on the same graph. In the ToF-SIMS negative ion depth profiles, the Fe_2^- signal is characteristic of the metallic substrate and the beginning of the intensity plateau is used to localize the metal and oxide/hydroxide layer interface. The FeO_2^- and Cl^- signals [48,49] indicate iron oxide/hydroxide [50,51] and chloride ions/iron chloride intermediates [52,53], respectively. The exact composition of these intermediates is not readily known, but their presence on the surface of iron/steel corroding in acidic aqueous solutions is also evidenced by electrochemical studies [50,52,53]. The $FeCO_2^-$ signal is used to indicate iron carbonate. On ToF-SIMS positive depth profiles, both the $C_{16}H_{34}N^+$ and $C_{23}H_{42}N^+$ signals represent the BDA-C14 inhibitor.

The ToF-SIMS depth profile of the native layer formed in air on 1018 carbon steel is shown in Fig. 4(a). Its comparison with depth profiles recorded after immersion in the NaCl solution with various concentrations of inhibitors will reveal the effect of the inhibitor on the nature, structure, composition and thickness of the surface layer. On the native surface, the FeO_2^- signal is spread over the first 50 s of sputtering,

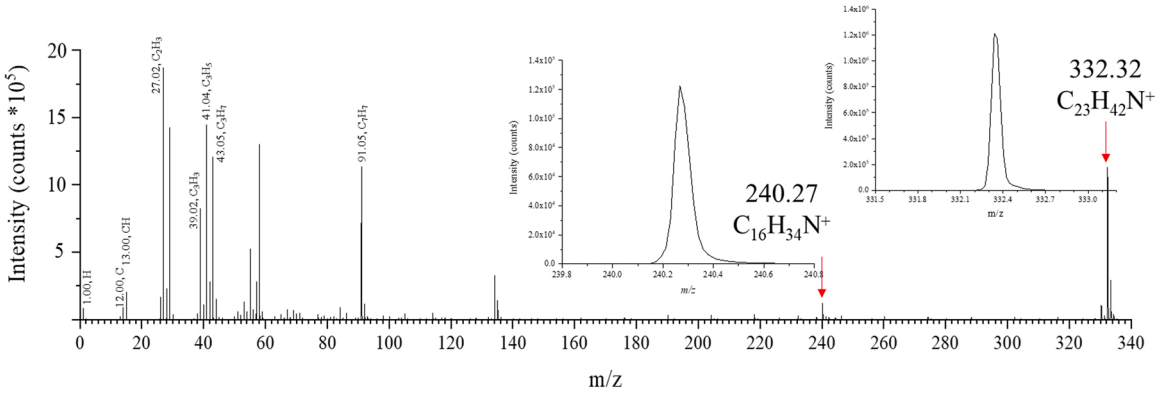

Fig. 2. ToF-SIMS positive ion spectrum for BDA-C14 inhibitor deposited on a silicon plate.

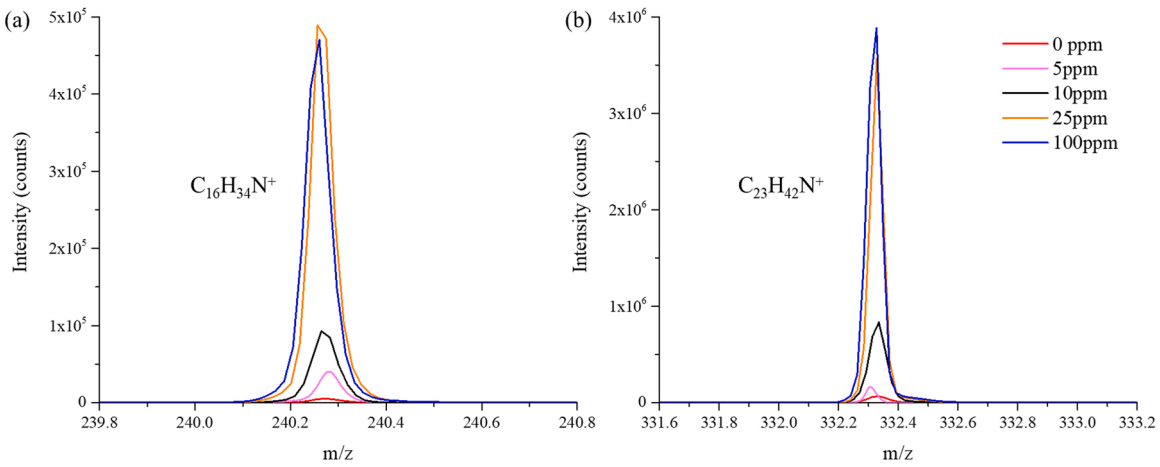

Fig. 3. ToF-SIMS positive ion mass spectra: (a) $C_{16}H_{34}N^+$ and (b) $C_{23}H_{42}N^+$, obtained on 1018 carbon steel after immersion for 1 h in 1 wt% NaCl solution saturated CO_2 with different BDA-C14 concentrations.

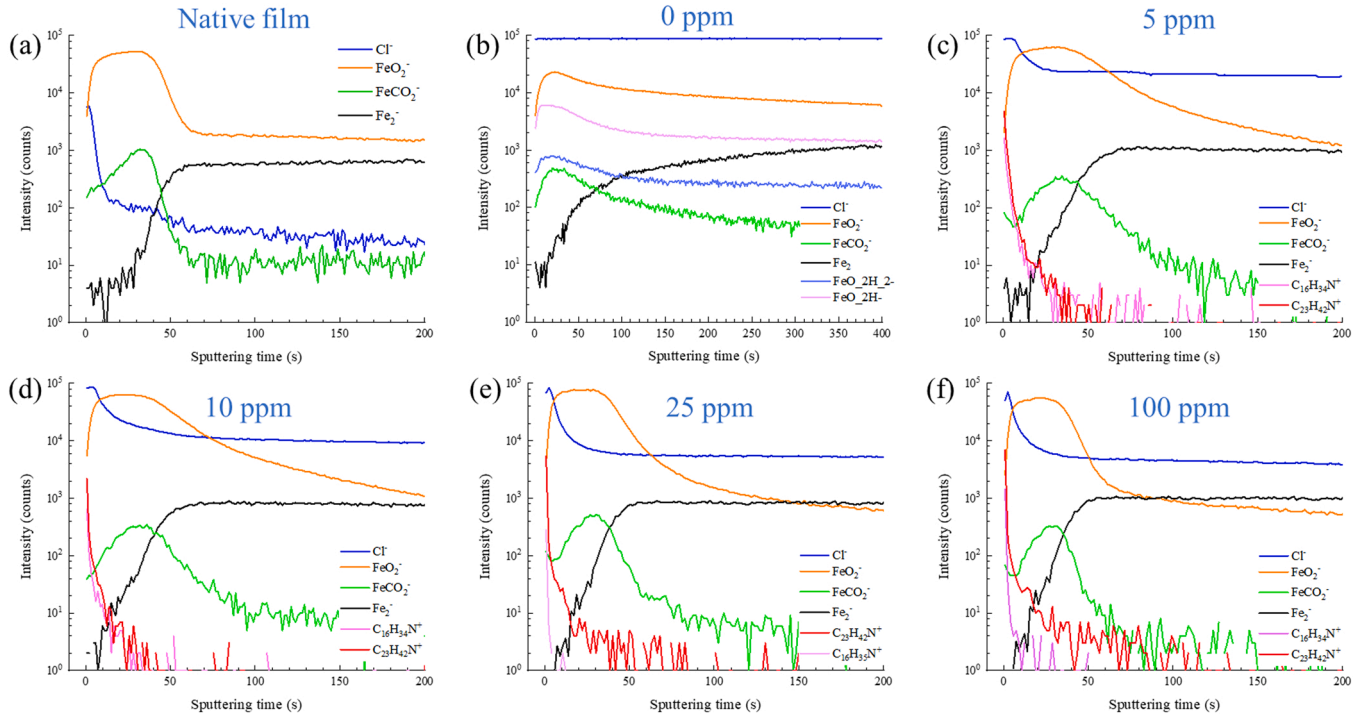

Fig. 4. ToF-SIMS depth profiles (for negative and positive ions) for layers formed on 1018 carbon steel (a) before and (b)-(f) after immersion for 1 h in 1 wt% NaCl solution saturated with CO_2 and with different BDA-C14 inhibitor concentrations: (b) 0 ppm_w, (c) 5 ppm_w, (d) 10 ppm_w, (e) 25 ppm_w and (f) 100 ppm_w.

indicating the presence of an iron oxide/hydroxide. As one probes deeper into the substrate, one enters a region which is characterized by the intense Fe_2^- signal. This second region corresponds to the metallic substrate. A small $FeCO_2^-$ signal is observed in the inner oxide layer, close to the metal and oxide/hydroxide layer interface. The intensity of this signal, much lower than the intensity of the FeO_2^- signal, indicates that traces of $FeCO_3$ coexist with the iron oxide/hydroxide in the inner region of the layer. Before immersion in NaCl containing solution, a Cl^- signal is observed during the first seconds of sputtering. It is not surprising considering the very high ionization yield of Cl in negative polarity. The Cl^- signal is thus assigned to a chloride contamination of the surface during surface preparation, removed after a few seconds of sputtering. A similar observation has been reported for other metal surfaces [54]. Fig. 4(b) shows the ToF-SIMS depth profiles obtained on carbon steel after 1 h immersion in CO_2 saturated NaCl solution without inhibitor. The FeO_2^- peaks before 50 s and the intense Fe_2^- ions in a deeper region indicate that the metallic substrate is still covered with a layer of iron oxide/hydroxide. Traces of $FeCO_3$ are also observed, as indicated by the low intensity $FeCO_2^-$ signal located close to the metal and oxide/hydroxide layer interface. The immersion in CO_2 saturated solution for relatively short exposure time has very limited effect on the amount of $FeCO_3$ in the surface layer. The Fe_2^- signal progressively increases but does not reach an intensity plateau even after 400 s of sputtering, and the FeO_2^- signal shows a slow intensity decreasing after 20 s of sputtering. This indicates a marked roughening of the surface, attributed to corrosion in the aqueous solution. Such observation has already been reported for other metals [48]. Focusing on the Cl^- signal, a constant intensity, around 10^5 counts, is observed throughout the whole probed thickness, due to the saturation of the detector (which is function of the ToF-SIMS analysis conditions). This indicates that the surface

layer formed on the carbon steel substrate contains a high concentration of Cl ions, and confirms that the specimen is significantly corroded when immersed in 1 wt% NaCl aqueous solution without inhibitor. The above discussed behaviors of FeO_2^-, Fe_2^- and Cl^- signals can be related with the iron dissolution mechanisms deduced from electrochemical studies. Several studies [55–57] have reported that there are two parallel reaction pathways in the mechanism for iron dissolution in chloride containing acidic media, one involving the formation of hydroxide intermediates and another involving chloride intermediates.

Fig. 4(c–f) shows the ToF-SIMS depth profiles recorded at various concentrations of inhibitor ranging from 5 ppm_w to 100 ppm_w on 1018 carbon steel immersed in 1 wt% NaCl aqueous solution, saturated with CO_2. Looking at the $C_{16}H_{34}N^+$ and $C_{23}H_{42}N^+$ signals, the depth profiles show that their maximum intensities are located at the outer surface leading to the conclusion that the Fe oxide/hydroxide (still characterized by the FeO_2^- signal) is covered by inhibitor molecules. Adsorption of BDA-C14 inhibitor is detected at 5 ppm_w and one observes that the thickness of the inhibitor layer remains unmodified at higher inhibitor concentrations. The $C_{16}H_{34}N^+$ and $C_{23}H_{42}N^+$ signals remain intense on the outer oxide/hydroxide surface only and decrease rapidly upon ion etching.

The in-depth profiles for the Cl^-, FeO_2^- and Fe_2^- negative ions obtained in the presence of the inhibitor are then compared to the in-depth profile obtained on the native layer in order to evaluate the protective effect of the adsorbed organic layer formed on the surface for various inhibitor concentrations in the aqueous solution. The observation of the FeO_2^- and Fe_2^- depth profiles allows us to conclude that after immersion in 1 wt% NaCl solution containing inhibitor, an oxide/hydroxide layer remains on the metallic substrate. The metal and oxide/hydroxide layer interface (assigned to the position where Fe_2^- reaches an intensity plateau) is located at 70 s, 60 s and 50 s of sputtering for inhibitor concentrations of 5 ppm_w, 10 ppm_w and 25 ppm_w and above, respectively. Thus, although with inhibitor concentrations lower than 25 ppm_w longer sputtering times required to remove the oxide/hydroxide are observed, one observes that the oxide/hydroxide layer thickness for inhibitor concentrations of 25 ppm_w and up is similar to the one observed on the native oxide/hydroxide layer, with a sharper metal and oxide/hydroxide layer interface. This indicates that a critical inhibitor concentration, around 25 ppm_w, is necessary to prevent corrosion of the 1018 carbon steel in 1 wt% NaCl solution, and thus limits the roughening caused by corrosion, which is responsible for a longer sputtering time. The roughness is also reflected by the long "tail" of the FeO_2^- signal into the metallic substrate region, which also supports the above interpretation. Finally, the high intensity of the Cl^- signal saturating the detector for the lowest inhibitor concentrations shows that for lower inhibitor concentration, iron dissolution still proceeds significantly as indicated by the accumulation of Cl^- and intermediates. The low concentration is not enough to form a protective barrier on the whole surface, therefore the surface is exposed to corrosive species in aqueous solution and therefore became roughened (as indicated by the thicker and less sharp FeO_2^- signal at 5 and 10 ppm_w) due to corrosion. The Cl^- and OH^- ions can adsorb and penetrate through the exposed surface layer, and then participate in the iron dissolution reactions. This study demonstrates that a critical inhibitor concentration exists for this chemical and that it is around 25 ppm_w. It corresponds to the bulk inhibitor concentration at which the surface has reached its maximum coverage by the inhibitor molecules. At this critical concentration (25 ppm_w) and above it, the oxide/hydroxide layer thickness remains similar to the one observed on the native surface. This indicates that the inhibitor layer is formed on the oxide/hydroxide layer surface, stabilizes it and strongly reduces the corrosion when the carbon steel is immersed in the aqueous solution. This critical inhibitor concentration is also consistent with the previous AFM observation [33] and electrochemical corrosion rates [33,47] results within a reasonable small deviation.

Since a critical inhibitor concentration enhances the corrosion protection of 1018 carbon steel immersed in 1 wt% NaCl solution saturated with CO_2, it is interesting to investigate the effect of exposure time to the inhibitor solution for this critical concentration. Thus, specimens were immersed in 1 wt% NaCl + 25 ppm_w BDA-C14 solution for durations ranging from 3 min to 3 h. Fig. 5 presents the intensities of the ToF-SIMS peaks related to $C_{16}H_{34}N^+$ and $C_{23}H_{42}N^+$ ions (characteristic of the inhibitor, see above) obtained on the surface of the 1018 carbon steel after different immersion times. For each specimen, and each immersion time, five different areas with a size of 500 × 500 μm^2 were analysed for statistics, and the lowest intensity values (red curves) and highest intensity values (black curves) are plotted in Fig. 5.

We observe a significant difference between the highest and the lowest intensity of the signals of the $C_{16}H_{34}N^+$ and $C_{23}H_{42}N^+$ ions for short immersion times, and this difference gradually decreases as immersion time increases. This indicates a non-uniform coverage by the inhibitor for short immersion times, whereas the coverage becomes uniform for longer times. Remarkably, the highest intensities (black curves) are similar for all immersion times (about 5×10^5 and 4×10^6 for $C_{16}H_{34}N^+$ and $C_{23}H_{42}N^+$, respectively), suggesting that densely covered regions on the surface already exist starting from 3 min of immersion. This is reasonable because it is well known that the kinetics of inhibitor adsorption via the positively charged headgroups is fast, as observed for the same inhibitor model compound by previous AFM [33], quartz crystal microbalance (QCM) [58] and electrochemical studies [33,47]. For example, it has been shown by in situ AFM real time topography imaging [33] that carbon steel surfaces corrode significantly within a few minutes after immersing in inhibitor solution, while further continuous corrosion could hardly be detected as immersion time increased, indicating inhibitor adsorption occurred just within a few minutes of immersion of steel. Likewise, some QCM studies [58–60] have detected the adsorption of inhibitor on metal surfaces after exposure for a few minutes. Also, the observed shift of the open circuit potential towards positive potentials immediately after injection of inhibitor indicates a fast adsorption [61,62]. Looking closer at the lowest intensity of the signals of the $C_{16}H_{34}N^+$ and $C_{23}H_{42}N^+$ ions on Fig. 5 (red plots), i.e., at the regions not densely covered by the adsorbed inhibitor molecules after short immersion times, it is observed that these regions start with low intensities, and their intensities slowly grow as immersion time increases until a uniform inhibitor layer formed. Combining this finding with the rapid adsorption observed at the highest intensity region (black curve) as discussed in last paragraph, it is consistent with previous studies [63–66], where the adsorption of surfactant molecules starts with a rapid adsorption thanks to electrostatic interactions between N containing polar head group and the surface, then followed by the progressive lateral growth of these adsorbed region by lateral hydrophobic interactions between molecular alkyl tails to form islands that, at the end, extend and form a close-packed layer of adsorbed inhibitor on the surface. Previous AFM studies of BDA-C14 inhibitor layers [32] and molecular simulation studies [67,68] also revealed this rapid adsorption followed by slow lateral self-assembly process.

ToF-SIMS in-depth profiles were also recorded on the 1018 carbon steel after immersion in 1 wt% NaCl solution with 25 ppm_w BDA-C14 for different times to investigate the effect of a uniform and compact inhibitor layer formation on the corrosion protection of carbon steel, and the results are presented in Fig. 6. The $C_{16}H_{34}N^+$ and $C_{23}H_{42}N^+$ depth profiles show that for all exposure times an inhibitor layer is adsorbed on outside surface of the oxide/hydroxide layer and the thickness of the inhibitor layer remains unchanged with exposure time. The similar shape of depth profiles for Fe_2^- and FeO_2^- signals suggests relatively low corrosion rates during immersion at all times. Another interesting point is that the plateau intensity variations for the Cl^- depth profiles, which increases from 10 counts at 0 min immersion (Fig. 4(a)) to 10^3 counts at 3 min, and then maintains stable at 10^4 counts after 1 h immersion, reveal that a continuous Cl^- diffusion into the oxide/hydroxide layer and formation of Cl intermediates through iron dissolution reaction take place for short immersion time and is then almost stopped after 1 h.

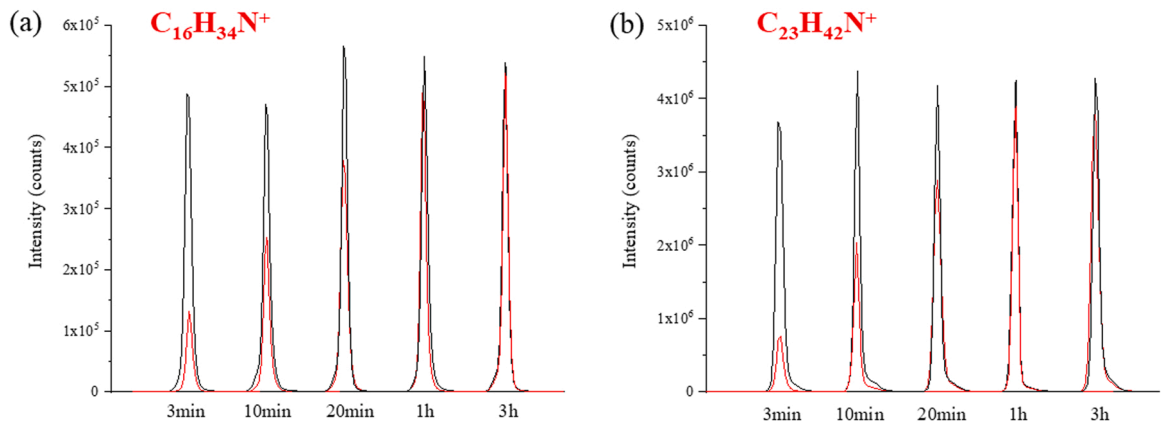

Fig. 5. ToF-SIMS positive ion mass spectra of (a) $C_{16}H_{34}N^+$ and (b) $C_{23}H_{42}N^+$, obtained for the 1018 carbon steel after immersion in 1 wt% NaCl and 25 ppm_w BDA-C14 solution saturated with CO_2, after different immersion times. (The red and black curves represent the lowest and highest intensity values obtained on the specimen surface at each immersion time).

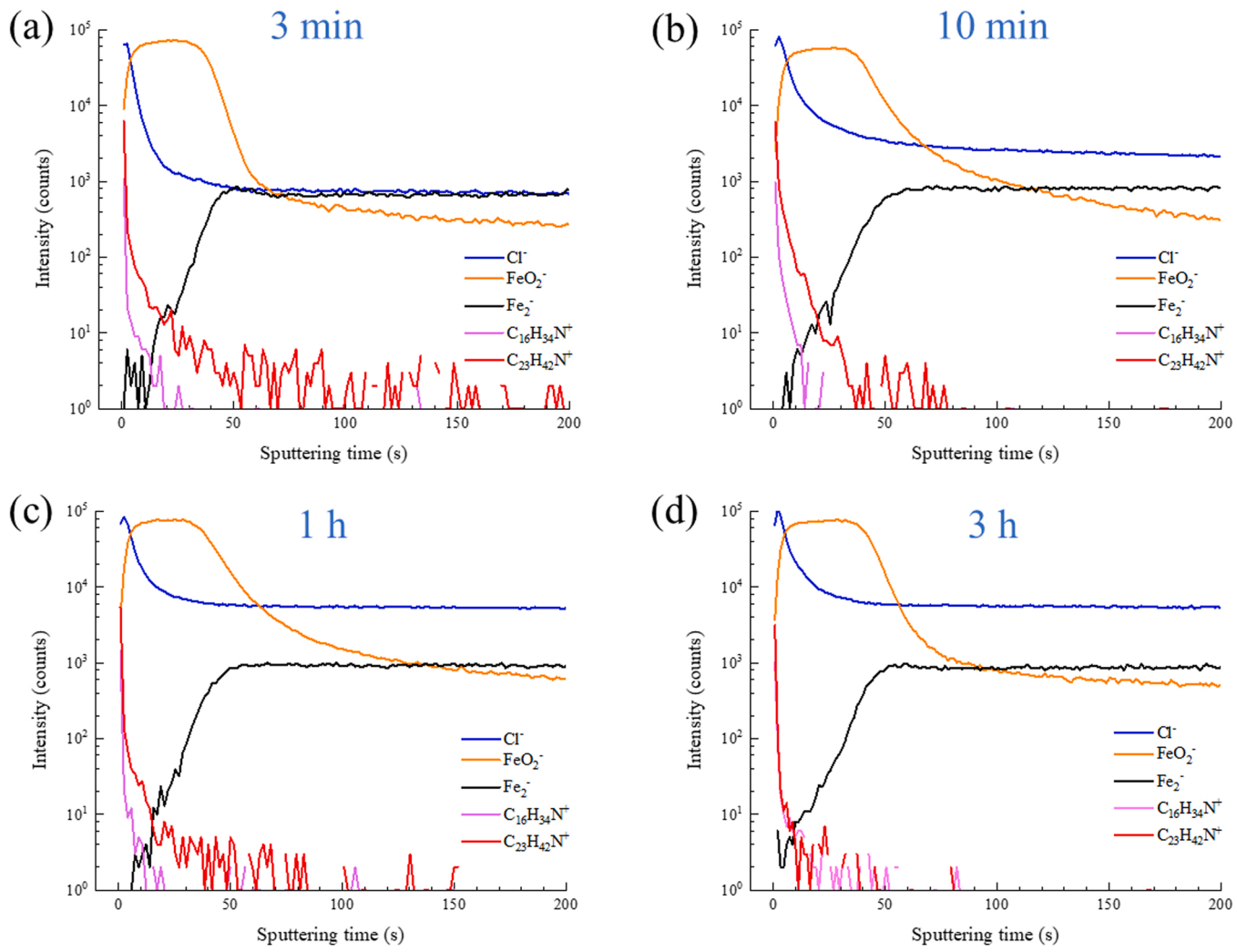

Fig. 6. ToF-SIMS negative and positive ions in-depth profiles for 1018 carbon steel after immersion in 1 wt% NaCl solution saturated with CO_2 with 25 ppm_w BDA-C14 inhibitor concentration for different immersion times: (a) 3 min, (b) 10 min, (c) 1 h and (d) 3 h.

Combining the discussion on the critical concentration (previous part) and the adsorption kinetics of the inhibitor layer on surface, one can conclude that, for short immersion time, a competition between the inhibitor adsorption and formation of Cl intermediates happens at the surface. With increasing immersion time, the formation of a compact and continuous inhibitor layer on the surface reduces the Cl adsorption and diffusion through oxide/hydroxide layer and further mitigate the formation of reaction intermediates.

XPS measurements were performed to obtain data on adsorption of the inhibitor on the carbon steel surface. Firstly, pure BDA-C14 inhibitor was analysed by XPS to get the basic chemical information. Fig. 7 shows the XPS high resolution spectra of C 1s and N 1s obtained on pure BDA-C14 inhibitor. The C 1s core level spectrum is fitted with two peaks (C1 and C2) at binding energies of 285.8 eV and 287.1 eV with peak areas of 93877 cps x eV and 22709 cps x eV, respectively. The N 1s core level spectrum is fitted with only one peak (N1) at a binding energy of 403.2 eV, with peak area of 8233 cps x eV. The atomic composition given directly by Avantage software after XPS peak fitting (the transmission, escape depth and sensitivity of each element were taken into account by the software) is C1: 78.4 %, C2: 17.4 % and N1: 4.2 %, and the ratio between carbon and nitrogen is 22.8, in agreement with the stoichiometric ratio calculated from the number of nitrogen (1) and carbon (23) atoms in the BDA-C14 molecule. In addition, the experimental atomic ratio between C2 and N1 is 4.1, in agreement with the assignment of C2 to the four carbon atoms bonded to nitrogen in the functional headgroup.

Fig. 8 shows the XPS high resolution spectra of Fe $2p_{3/2}$, N 1s and C 1s obtained for 1018 carbon steel before and after 1 h immersion in 1 wt % NaCl solution with inhibitor concentrations of 0, 25, and 100 ppm_w. The C 1s spectra are fitted with four peaks, corresponding to the C-C/C-H (BE = 285 eV), C-O and C-N (BE = 286.3 eV), O-C-O (BE = 288.2 eV) and O-C═O (BE = 289.1 eV). No iron carbonate species are observed in the C 1s spectra, indicating that if there is any $FeCO_3$, its concentration in the surface oxide/hydroxide layer is below 1 % (detection limit of XPS). The C 1s spectra are not used to characterize the inhibitor, since they contain the signals of adventitious carbonaceous species. The Fe $2p_{3/2}$ spectra are fitted with two peaks, corresponding to metallic Fe (BE = 706.6 eV) and oxidized Fe(II/III) (BE = 710.3 ± 0.2 eV). For the native layer, i.e. before immersion (Fig. 8(a2)) and for the specimen immersed in pure NaCl solution (without inhibitor) (Fig. 8(b2)), a single peak at a binding energy of 400.1 eV allows us to fit the N 1s spectra. The intensity of this peak is very low, and can be assigned to some surface organic contamination or nitrogen in the carbon steel (although the very low nitrogen content in the steel makes this unlikely). After immersion in NaCl solution with addition of 25 ppm_w and 100 ppm_w inhibitor, the N1s peak intensities are higher and three peaks are necessary to fit the N 1s spectra. Among these three peaks, the one at a binding energy of 400 eV is assigned to nitrogen from some surface organic contamination or the nitrogen in carbon steel. The two others, at binding energies of 403.2 eV and 398.1 eV are assigned to the inhibitor adsorbed on the surface. It is noted that the peak at 403.2 eV corresponds to the exact same binding energy as that observed for the pure inhibitor adsorbed on silicon wafer (Fig. 7), and thus it is assigned to physisorbed inhibitor.

As for the peak at 398.1 eV, the situation is more complicated and the different possibilities are discussed below. The first considers a scenario that is related to two different molecular orientations of the benzene ring. Khan et al. [69] did an all-atom molecular dynamics simulation for the BDA series inhibitor molecules. The simulation results showed the benzene ring could have strong affinity to metal surface, and tends to lie flat on the surface, perhaps with π-electrons interacting with metal [10]. The bond of the benzene ring with surface may change the electronic density of N in the molecule. Therefore, the two different molecular orientations of benzene ring (bonded to surface or not), may induce these two different N binding energies at 403.2 eV and 398.1 eV. Second scenario involves two different molecular orientations for head groups and tails. Based on Ko et al.'s [68] molecular dynamic simulation, the amphiphilic inhibitor molecules adsorb on surface with their polar head and hydrophobic tails towards the surface alternately, when forming a uniform layer. This could give two different binding energies for N because one type of molecules has its N atom electrostatically interacting with the surface (head group towards surface), and another type of molecules has its N atom towards the bulk without interaction with the surface (head group towards bulk). Interestingly, Wu et al. [70] have also found that for a 2-mercaptobenzimidazole (2-MBI) inhibitor molecule adsorbed on copper, the N 1s spectrum is composed of two components N1 and N2 at binding energies of 400.1 eV and 398.9 eV, corresponding to nitrogen bonded and not bonded to copper, respectively. One can also easily assign these two different binding energies as physisorption and chemisorption, however, BDA-C14 inhibitor as a quaternary ammonium compound does not have lone pair electrons on its N, therefore it is hard to imagine it can form a chemical bond with the steel surface. Therefore, this scenario is unlikely, and the first two scenarios with different molecular orientations are more plausible to explain the two peaks of N at 403 eV and 398.1 eV.

The peak area ratio between nitrogen species (N (403 eV) / N (398.1 eV)) is the same for two different concentrations, showing that when the surface of the carbon steel is fully covered by the inhibitor, the ratio between molecules with two different orientations remains constant. The mechanism of inhibitor adsorption strongly depends on the surface/inhibitor system. In the case of inhibitors with nitrogen-containing functional headgroups, the inhibitor adsorption can be by electrostatic interactions between N head group and steel surface with different molecular orientations [10–12,71].

Based on the ToF-SIMS in-depth profiles, a model of the inhibitor/oxide/metal system covering the carbon steel substrate is proposed and is presented Fig. 9. It is then used to calculate, from the XPS data, the inhibitor and oxide/hydroxide layer thicknesses. To do so, it is assumed that a continuous and compact oxide/hydroxide layer is formed on the metallic substrate, and that the inhibitor layer covers the oxide/hydroxide layer. Thus, the thickness can be calculated from the following set of equations (for an analysis take-off angle of 90°):

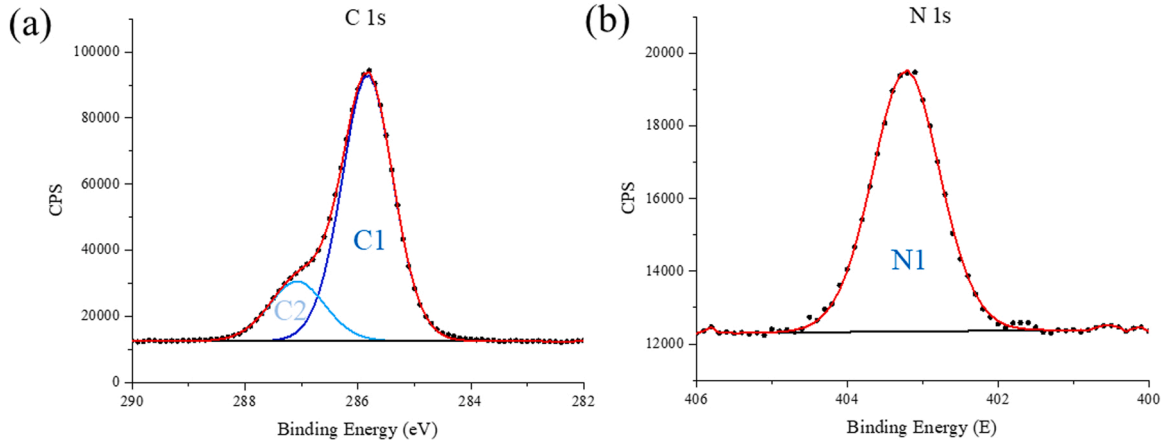

Fig. 7. XPS high resolution spectra of (a) C 1s and (b) N 1s obtained for pure BDA-C14 inhibitor.

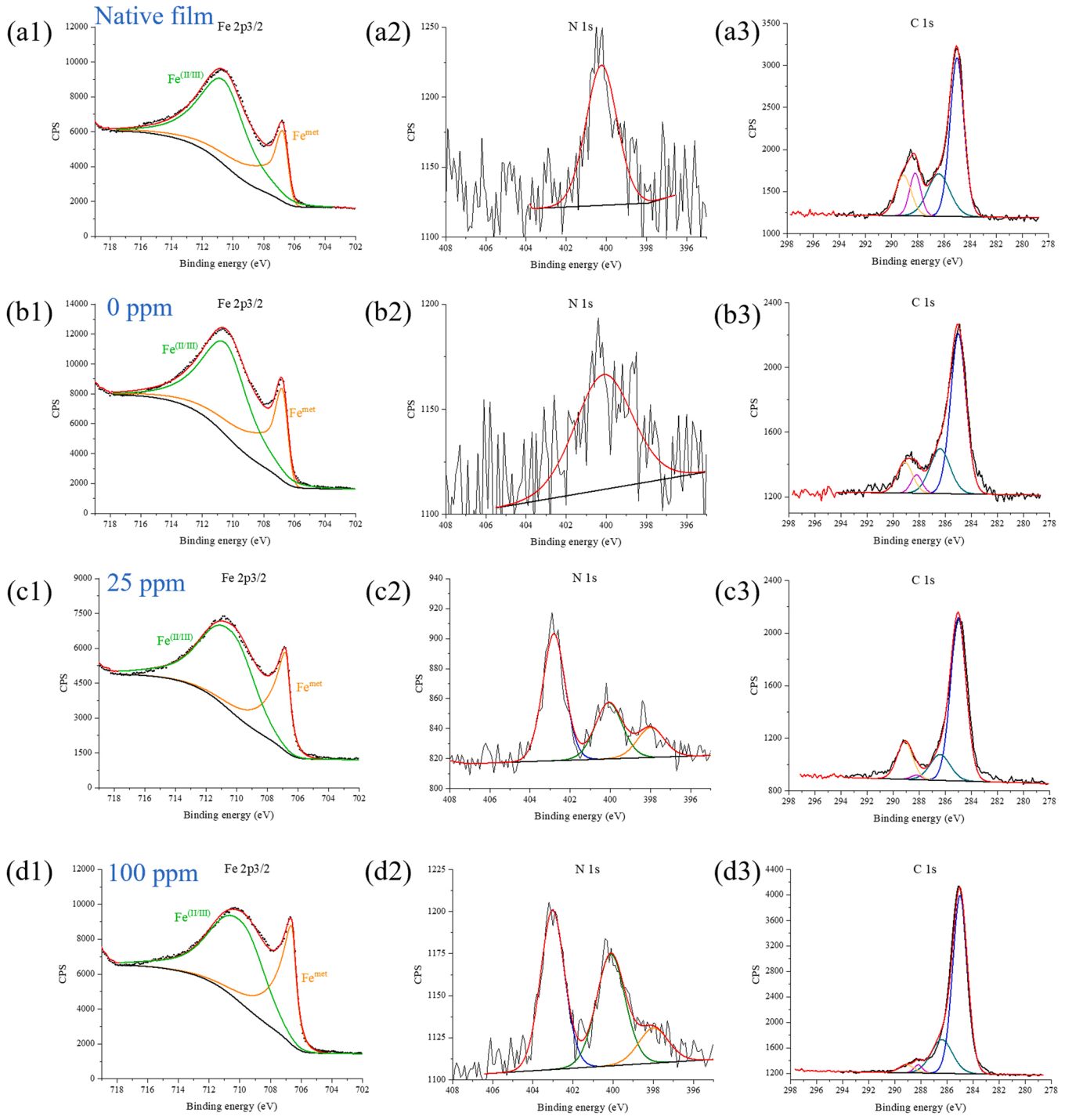

Fig. 8. XPS high resolution spectra of (a1-d1) Fe 2p3/2, (a2-d2) N 1s and (a3-d3) C 1s obtained for 1018 carbon steel (a) before (native layer) and after 1 h immersion in 1 wt% NaCl solution with various BDA-C14 inhibitor concentrations ((b) 0 ppm_w, (c) 25 ppm_w, (d) 100 ppm_w).

$$I_{Fe}^{Oxide} = k\sigma_{Fe}\lambda_{Fe}^{Oxide}D_{Fe}^{Oxide}T_{Fe}\exp\left(-\frac{d_{inhibitor}}{\lambda_{Fe}^{inhibitor}}\right)\left[1-\exp\left(-\frac{d_{oxide}}{\lambda_{Fe}^{oxide}}\right)\right] \quad (1)$$

$$I_{N}^{Inhibitor} = k\sigma_{N}\lambda_{N}^{Inhibitor}D_{N}^{Inhibitor}T_{N}\left[1-\exp(-\frac{d_{Inhibitor}}{\lambda_{N}^{Inhibitor}})\right] \quad (2)$$

$$I_{Fe}^{Metal} = k\sigma_{Fe}\lambda_{Fe}^{Metal}D_{Fe}^{Metal}T_{Fe}\exp\left(-\frac{d_{oxide}}{\lambda_{Fe}^{Oxide}}\right)\exp\left(-\frac{d_{inhibitor}}{\lambda_{N}^{Inhibitor}}\right) \quad (3)$$

where I is the intensity of the photoelectrons, k is the constant dependent of the spectrometer, T_x is the transmission factor of the considered core level X, λ is the inelastic mean free path of an element estimated using the TPP2M [72], D is the density of the element, σ is the photoionization cross section of the element taken from Scofield [73], d is the thickness of the layer.

The thickness of the oxide/hydroxide layer is estimated to 2.7 nm for the native layer, 2.9 nm for the specimen immersed in inhibitor free NaCl solution, and 2.6 nm for the specimen immersed in inhibitor (25 ppm_w and 100 ppm_w) containing NaCl solutions. The oxide/hydroxide layer thickness remains similar whatever the treatment given to the substrate. Concerning the inhibitor layer, a thickness of 0.15 nm is

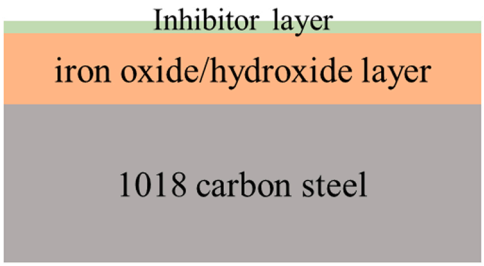

Fig. 9. Model used to calculate the thicknesses of inhibitor and oxide/hydroxide layers on a 1018 carbon steel surface, based on the ToF-SIMS results.

calculated for the two specimens exposed to the inhibitor-containing solutions (25 ppm_w and 100 ppm_w). Considering the molecular tail length of BDA-C14, i.e. 1.64 nm (obtained from Avogadro software, or calculated from the 0.154 nm carbon-carbon bond length and 109°28′ bonding angle), one concludes that the inhibitor molecule (and particularly the long alkyl chains) are oriented along the substrate surface or tilted with an estimated angle of 5° between the molecule and the surface, i.e. the inhibitor molecules are adsorbed in the "lying down" position. Considering the van der Waals radius of carbon atoms of 0.170 nm [74], the lying down adsorption seems to be the most likely inhibitor molecule orientations at the surface as analysed by XPS. This result is different from the one obtained by AFM on mica that concluded to a more tilted orientation of BDA-C14 inhibitor with 1–1.5 nm layer thickness [32]. The apparent smaller layer thickness calculated from XPS data can also be related to the simplified model used for the calculation and/or a possible dehydration when introducing the specimen into the ultra-high vacuum chamber that could result in the collapse of the inhibitor alkyl chains on the surface, while the AFM measurements were performed in aqueous solution and inhibitor alkyl tail tended to "stand up" due to hydrophobic interactions.

4. Conclusions

This study reports the investigation of adsorption of BDA-C14 molecule for corrosion inhibition of 1018 carbon steel in CO_2 saturated 1 wt% NaCl solution. Direct evidence of the inhibitor adsorption on the steel surface is provided by ToF-SIMS and XPS surface analyses. XPS detects N-containing polar head groups with two binding energies at 403.2 eV and 398.1 eV compared to the reference molecule with only one binding energy at 403.2 eV. This indicates that interactions between inhibitor and steel surface are assigned to two possibly different molecular orientations of benzene ring or headgroup. The thickness of the full inhibitor layer is estimated to be about 0.15 nm. This is consistent with the adsorption of flat-lying molecules on the steel surface. ToF-SIMS mass spectra and in-depth profiles confirm that the BDA-C14 corrosion inhibitor is adsorbed on the carbon steel surface, and the critical concentration for inhibitor adsorption and corrosion protection is about 25 ppm_w in 1 wt% NaCl solution saturated with CO_2. When the inhibitor concentration is below 25 ppm_w, the amount of inhibitor is insufficient to get a full coverage of the steel surface and corrosion is observed on carbon steel. When the inhibitor concentration is above 25 ppm_w, the carbon steel is fully covered by the inhibitor and the carbon steel corrosion is remarkably reduced. This is the result of the formation of a compact and continuous inhibitor layer on the surface. Inhibitor concentrations higher than 25 ppm_w do not modify the nature, structure and thickness of the adsorbed organic layer on the steel surface.

The inhibitor adsorption kinetics on the carbon steel surface at 25 ppm_w concentration was also investigated by ToF-SIMS. For immersion times below 20 min, defective areas remain in the inhibitor layer where iron dissolution occurs with the formation of chloride/hydroxide intermediates. These defective areas are progressively sealed and a uniform and compact inhibitor layer covers the surface after 1 h of immersion time, mitigates the chloride diffusion through oxide/hydroxide layer and the formation of chloride/hydroxide intermediates.

CRediT authorship contribution statement

Luntao Wang: Investigation, Formal analysis, Visualization, Writing – original draft. **Huiru Wang:** Investigation, Formal analysis, Writing – review & editing. **Antoine Seyeux:** Validation, Investigation, Writing – review & editing. **Sandrine Zanna:** Validation, Investigation, Writing – review & editing. **Alain Pailleret:** Writing – review & editing. **Srdjan Nesic:** Supervision, Writing – review & editing. **Philippe Marcus:** Conceptualization, Funding acquisition, Supervision, Writing - review & editing.

Declaration of Competing Interest

The authors declare that they have no known competing financial interests or personal relationships that could have appeared to influence the work reported in this paper.

Data Availability

Data will be made available on request.

Acknowledgments

This project has received funding from the European Research Council (ERC) under the European Union's Horizon 2020 research and innovation program (ERC Advanced Grant No. 741123, Corrosion Initiation Mechanisms at the Nanometric and Atomic Scales: CIMNAS). Région Île-de-France is acknowledged for partial funding of the ToF-SIMS and XPS equipments. The author Huiru Wang is supported by National Science Foundation CBET grant 1705817. The authors also would like to thank Dr. David Young for helping synthesize inhibitor model compounds that have been used in this work as well as fragment analysis of inhibitor molecules and fruitful discussions regarding with the molecular orientations, thank Dr Sharma Sumit for the analysis of molecular orientations, also thank Dr Bruce Brown for helping fabricate the steel specimen.

References

[1] S. Peng, Z. Zhang, E. Liu, W. Liu, W. Qiao, A new hybrid algorithm model for prediction of internal corrosion rate of multiphase pipeline, J. Nat. Gas Sci. Eng. 85 (2021), 103716.
[2] J. Capelle, I. Dmytrakh, G. Pluvinage, Comparative assessment of electrochemical hydrogen absorption by pipeline steels with different strength, Corros. Sci. 52 (2010) 1554–1559.
[3] Y. Zhang, X. Pang, S. Qu, X. Li, K. Gao, Discussion of the CO_2 corrosion mechanism between low partial pressure and supercritical condition, Corros. Sci. 59 (2012) 186–197.
[4] M. Ilman, Analysis of internal corrosion in subsea oil pipeline, case studies in Engineering Failure Analysis, 2, 2014, pp. 1–8.
[5] Y. Chen, T. Hong, M. Gopal, W. Jepson, EIS studies of a corrosion inhibitor behavior under multiphase flow conditions, Corros. Sci. 42 (2000) 979–990.
[6] D. Zhang, L. Li, L. Cao, N. Yang, C. Huang, Studies of corrosion inhibitors for zinc–manganese batteries: quinoline quaternary ammonium phenolates, Corros. Sci. 43 (2001) 1627–1636.
[7] S. Ramachandran, V. Jovancicevic, Molecular modeling of the inhibition of mild steel carbon dioxide corrosion by imidazolines, Corrosion 55 (1999).
[8] J. Zhang, J. Liu, W. Yu, Y. Yan, L. You, L. Liu, Molecular modeling of the inhibition mechanism of 1-(2-aminoethyl)-2-alkyl-imidazoline, Corros. Sci. 52 (2010) 2059–2065.
[9] R.A. Sims, S.L. Harmer, J.S. Quinton, The role of physisorption and chemisorption in the oscillatory adsorption of organosilanes on aluminium oxide, Polymers 11 (2019) 410.
[10] M. Goyal, S. Kumar, I. Bahadur, C. Verma, E.E. Ebenso, Organic corrosion inhibitors for industrial cleaning of ferrous and non-ferrous metals in acidic solutions: a review, J. Mol. Liq. 256 (2018) 565–573.
[11] A. Edwards, C. Osborne, S. Webster, D. Klenerman, M. Joseph, P. Ostovar, M. Doyle, Mechanistic studies of the corrosion inhibitor oleic imidazoline, Corros. Sci. 36 (1994) 315–325.

[12] Y. Qiang, S. Zhang, L. Wang, Understanding the adsorption and anticorrosive mechanism of DNA inhibitor for copper in sulfuric acid, Appl. Surf. Sci. 492 (2019) 228–238.
[13] N. Kovačević, A. Kokalj, Chemistry of the interaction between azole type corrosion inhibitor molecules and metal surfaces, Mater. Chem. Phys. 137 (2012) 331–339.
[14] S. Michelhaugh, C. Bhardwaj, G. Cali, B. Bravo, M. Bothwell, G. Berry, M. Soriaga, The influence of chemisorbed organic monolayers on electrode surface oxidation, Corrosion 47 (1991) 322–328.
[15] M. Low, Kinetics of chemisorption of gases on solids, Chem. Rev. 60 (1960) 267–312.
[16] E. McCafferty, Introduction to Corrosion Science, Springer Science & Business Media, 2010, pp. 109–110.
[17] A. Javaid, S.O. Gonzalez, E.E. Simanek, D.M. Ford, Nanocomposite membranes of chemisorbed and physisorbed molecules on porous alumina for environmentally important separations, J. Membr. Sci. 275 (2006) 255–260.
[18] D.C. Turner, B.M. Peek, T.E. Wertz, D.D. Archibald, R.E. Geer, B.P. Gaber, Enzymatic modification of a chemisorbed lipid monolayer, Langmuir 12 (1996) 4411–4416.
[19] R. Gašparac, C. Martin, E. Stupnišek-Lisac, In situ studies of imidazole and its derivatives as copper corrosion inhibitors. I. Activation energies and thermodynamics of adsorption, J. Electrochem. Soc. 147 (2000) 548.
[20] A. Kokalj, S. Peljhan, M. Finsgar, I. Milosev, What determines the inhibition effectiveness of ATA, BTAH, and BTAOH corrosion inhibitors on copper? J. Am. Chem. Soc. 132 (2010) 16657–16668.
[21] R. De Marco, W. Durnie, A. Jefferson, B. Kinsella, A. Crawford, Persistence of carbon dioxide corrosion inhibitors, Corrosion 58 (2002) 354–363.
[22] Y.-J. Tan, S. Bailey, B. Kinsella, An investigation of the formation and destruction of corrosion inhibitor films using electrochemical impedance spectroscopy (EIS), Corros. Sci. 38 (1996) 1545–1561.
[23] M. Elayyachy, A. El Idrissi, B. Hammouti, New thio-compounds as corrosion inhibitor for steel in 1 M HCl, Corros. Sci. 48 (2006) 2470–2479.
[24] G. Moretti, F. Guidi, G. Grion, Tryptamine as a green iron corrosion inhibitor in 0.5 M deaerated sulphuric acid, Corros. Sci. 46 (2004) 387–403.
[25] T. Hong, Y. Sun, W. Jepson, Study on corrosion inhibitor in large pipelines under multiphase flow using EIS, Corros. Sci. 44 (2002) 101–112.
[26] Y. Qiang, S. Zhang, B. Tan, S. Chen, Evaluation of Ginkgo leaf extract as an eco-friendly corrosion inhibitor of X70 steel in HCl solution, Corros. Sci. 133 (2018) 6–16.
[27] W. Lorenz, F. Mansfeld, Interface and interphase corrosion inhibition, Electrochim. Acta 31 (1986) 467–476.
[28] C. Cao, On electrochemical techniques for interface inhibitor research, Corros. Sci. 38 (1996) 2073–2082.
[29] R. Zvauya, J. Dawson, Inhibition studies in sweet corrosion systems by a quaternary ammonium compound, J. Appl. Electrochem. 24 (1994) 943–947.
[30] J.D. Olivo, B. Brown, S. Nesic, Modeling of corrosion mechanisms in the presence of quaternary ammonium chloride and imidazoline corrosion inhibitors, Corrosion, 2016, paper no. 7406.
[31] Y. Xiong, B. Brown, B. Kinsella, S. Nesic, A. Pailleret, Atomic force microscopy study of the adsorption of surfactant corrosion inhibitor films, Corrosion 70 (2014) 247–260.
[32] H. Wang, B. Brown, S. Nesic, A. Pailleret, Investigation of Inhibitor Adsorption Mechanism by in Situ Tapping Mode Atomic Force Microscopy, CORROSION 2021, paper no. 16610.
[33] H. Wang, S. Sharma, A. Pailleret, B. Brown, S. Nesic, Investigation of corrosion inhibitor adsorption on mica and mild steel using electrochemical atomic force microscopy and molecular simulations, Corrosion 78 (2022) 978–990.
[34] X. Wu, F. Wiame, V. Maurice, P. Marcus, Adsorption and thermal stability of 2-mercaptobenzothiazole corrosion inhibitor on metallic and pre-oxidized Cu (1 1 1) model surfaces, Appl. Surf. Sci. 508 (2020), 145132.
[35] X. Wu, F. Wiame, V. Maurice, P. Marcus, 2-Mercaptobenzothiazole corrosion inhibitor deposited at ultra-low pressure on model copper surfaces, Corros. Sci. 166 (2020), 108464.
[36] I. Milošev, D. Zimerl, C. Carriére, S. Zanna, A. Seyeux, J. Iskra, S. Stavber, F. Chiter, M. Poberžnik, D. Costa, A. Kokalj, P. Marcus, Editors' choice—the effect of anchor group and alkyl backbone chain on performance of organic compounds as corrosion inhibitors for aluminum investigated using an integrative experimental-modeling approach, Journal of The Electrochemical Society, 167, 2020, p. 061509.
[37] I. Milošev, T. Bakarič, S. Zanna, A. Seyeux, P. Rodič, M. Poberžnik, F. Chiter, P. Cornette, D. Costa, A. Kokalj, P. Marcus, Electrochemical, surface-analytical, and computational DFT study of alkaline etched aluminum modified by carboxylic acids for corrosion protection and hydrophobicity, J. Electrochem. Soc. 166 (2019) C3131.
[38] M. Finšgar, Surface analysis and interface properties of 2-aminobenzimidazole corrosion inhibitor for brass in chloride solution, Anal. Bioanal. Chem. 412 (2020) 8431–8442.
[39] M. Finšgar, Electrochemical, 3D topography, XPS, and ToF-SIMS analyses of 4-methyl-2-phenylimidazole as a corrosion inhibitor for brass, Corros. Sci. 169 (2020), 108632.
[40] R. Gašparac, C.R. Martin, E. Stupnišek-Lisac, Z. Mandic, In situ and ex situ studies of imidazole and its derivatives as copper corrosion inhibitors. II. AC impedance, XPS, and SIMS studies, J. Electrochem. Soc. 147 (2000) 991.
[41] K. Marcoen, P. Visser, G.F. Trindade, M.-L. Abel, J.F. Watts, J.M. Mol, H. Terryn, T. Hauffman, Compositional study of a corrosion protective layer formed by leachable lithium salts in a coating defect on AA2024-T3 aluminium alloys, Prog. Org. Coat. 119 (2018) 65–75.
[42] P. Visser, K. Marcoen, G. Trindade, M. Abel, J. Watts, T. Hauffman, J. Mol, H. Terryn, The chemical throwing power of lithium-based inhibitors from organic coatings on AA2024-T3, Corros. Sci. 150 (2019) 194–206.
[43] P. Morales-Gil, M. Walczak, R. Cottis, J. Romero, R. Lindsay, Corrosion inhibitor binding in an acidic medium: Interaction of 2-mercaptobenizmidazole with carbon-steel in hydrochloric acid, Corros. Sci. 85 (2014) 109–114.
[44] M.S. Walczak, P. Morales-Gil, T. Belashehr, K. Kousar, P.A. Lozada, R. Lindsay, Determining the chemical composition of corrosion inhibitor/metal interfaces with XPS: minimizing post immersion oxidation, J. Vis. Exp. (2017), e55163.
[45] K. Kousar, M. Walczak, T. Ljungdahl, A. Wetzel, H. Oskarsson, P. Restuccia, E. Ahmad, N. Harrison, R. Lindsay, Corrosion inhibition of carbon steel in hydrochloric acid: Elucidating the performance of an imidazoline-based surfactant, Corros. Sci. 180 (2021), 109195.
[46] N. Moradighadi, S. Lewis, J.D. Olivo, D. Young, B. Brown, S. Nešić, Determining critical micelle concentration of organic corrosion inhibitors and its effectiveness in corrosion mitigation, Corrosion 77 (2021) 266–275.
[47] J.D. Olivo, B. Brown, D. Young, S. Nešić, Effect of corrosion inhibitor alkyl tail length on the electrochemical process governing CO_2 corrosion of mild steel, Corrosion 75 (2019) 137–139.
[48] Z. Wang, A. Seyeux, S. Zanna, V. Maurice, P. Marcus, Chloride-induced alterations of the passive film on 316L stainless steel and blocking effect of pre-passivation, Electrochim. Acta 329 (2020), 135159.
[49] L. Wang, A. Seyeux, P. Marcus, Thermal stability of the passive film formed on 316L stainless steel surface studied by ToF-SIMS, Corros. Sci. 165 (2019), 108395.
[50] B. JO'M, D. Drazic, A. Despic, The electrode kinetics of the deposition and dissolution of iron, Electrochim. Acta 4 (1961) 325–361.
[51] K.E. Heusler, Encyclopedia of Electrochemistry of the Elements, 9, Marcel Dekker, New York, NY, 1982, pp. 229–381.
[52] D.M. Drazic, Iron and its electrochemistry in an active state, in Modern Aspects of Electrochemistry. Modern Aspects of Electrochemistry, Springer, Boston, MA, 1989, pp. 69–192.
[53] N. Darwish, F. Hilbert, W. Lorenz, H. Rosswag, The influence of chloride ions on the kinetics of iron dissolution, Electrochim. Acta 18 (1973) 421–425.
[54] Z. Wang, E.M. Paschalidou, A. Seyeux, S. Zanna, V. Maurice, P. Marcus, Mechanisms of Cr and Mo enrichments in the passive oxide film on 316L austenitic stainless steel, Front. Mater. 6 (2019) 232.
[55] R.J. Chin, K. Nobe, Electrodissolution kinetics of iron in chloride solutions: III. Acidic solutions, J. Electrochem. Soc. 119 (1972) 1457.
[56] H. Kuo, K. Nobe, Electrodissolution kinetics of iron in chloride solutions: VI. Concentrated acidic solutions, J. Electrochem. Soc. 125 (1978) 853.
[57] K. Heusler, G. Cartledge, The influence of iodide ions and carbon monoxide on the anodic dissolution of active iron, J. Electrochem. Soc. 108 (1961) 732.
[58] K. Singla, H. Perrot, O. Sel, B. Brown, S. Nesic, Use of Quartz Crystal Microbalance in Study of Inhibitor Adsorption, Corrosion, 2021, paper no. 16653.
59] M. Knag, J. Sjöblom, G. Øye, E. Gulbrandsen, A quartz crystal microbalance study of the adsorption of quaternary ammonium derivates on iron and cementite, Colloids Surf. A: Physicochem. Eng. Asp. 250 (2004) 269–278.
[60] I. Jevremović, M. Singer, S. Nešić, V. Mišković-Stanković, Inhibition properties of self-assembled corrosion inhibitor talloil diethylenetriamine imidazoline for mild steel corrosion in chloride solution saturated with carbon dioxide, Corros. Sci. 77 (2013) 265–272.
[61] F. Zulkifli, M.S.M. Yusof, M. Isa, A. Yabuki, W.W. Nik, Henna leaves extract as a corrosion inhibitor in acrylic resin coating, Prog. Org. Coat. 105 (2017) 310–319.
[62] H. Amar, J. Benzakour, A. Derja, D. Villemin, B. Moreau, A corrosion inhibition study of iron by phosphonic acids in sodium chloride solution, J. Electroanal. Chem. 558 (2003) 131–139.
[63] W.A. Hayes, D.K. Schwartz, Two-stage growth of octadecyltrimethylammonium bromide monolayers at mica from aqueous solution below the Krafft point, Langmuir 14 (1998) 5913–5917.
[64] I. Doudevski, W.A. Hayes, D.K. Schwartz, Submonolayer island nucleation and growth kinetics during self-assembled monolayer formation, Phys. Rev. Lett. 81 (1998) 4927.
[65] J. Woodward, I. Doudevski, H. Sikes, D. Schwartz, Kinetics of self-assembled monolayer growth explored via submonolayer coverage of incomplete films, J. Phys. Chem. B 101 (1997) 7535–7541.
[66] Y. Rabinovich, J. Kanicky, S. Pandey, H. Oskarsson, K. Holmberg, B. Moudgil, D. Shah, Self-assembled Gemini surfactant film-mediated dispersion stability, J. Colloid Interface Sci. 288 (2005) 583–590.
[67] S. Sharma, H. Singh, X. Ko, A quantitatively accurate theory to predict adsorbed configurations of linear surfactants on polar surfaces, J. Phys. Chem. B 123 (2019) 7464–7470.
[68] X. Ko, S. Sharma, Adsorption and self-assembly of surfactants on metal–water interfaces, J. Phys. Chem. B 121 (2017) 10364–10370.
[69] M.R. Khan, H. Singh, S. Sharma, K.L. Asetre Cimatu, Direct Observation of Adsorption Morphologies of Cationic Surfactants at the Gold Metal–Liquid Interface, J. Phys. Chem. Lett. 11 (2020) 9901–9906.
[70] X. Wu, F. Wiame, V. Maurice, P. Marcus, Effects of water vapour on 2-mercapto-benzothiazole corrosion inhibitor films deposited on copper, Corros. Sci. 189 (2021), 109565.
[71] A. Kokalj, Corrosion inhibitors: physisorbed or chemisorbed? Corros. Sci. 196 (2022), 109939.

[72] S. Tanuma, C.J. Powell, D.R. Penn, Calculations of electorn inelastic mean free paths. II. Data for 27 elements over the 50–2000 eV range, Surf. Interface Anal. 17 (1991) 911–926.
[73] J.H. Scofield, Hartree-Slater subshell photoionization cross-sections at 1254 and 1487 eV, J. Electron Spectrosc. Relat. Phenom. 8 (1976) 129–137.
[74] K. Ohno, H. Satoh, T. Iwamoto, H. Tokoyama, H. Yamakado, Wavy carbon: A new series of carbon structures explored by quantum chemical calculations, Chem. Phys. Lett. 639 (2015) 178–182.